Regulating Second-Harmonic Generation by van der Waals Interactions in Two-dimensional Lead Halide Perovskite Nanosheets

Wen-Juan Wei,[†,‡,§,∇] Xing-Xing Jiang,[∥,∇] Li-Yuan Dong,[‡] Wei-Wei Liu,[‡] Xiao-Bo Han,[‡,⊥] Yan Qin,[‡] Kai Li,[†] Wei Li,*[,†,‡] Zhe-Shuai Lin,*[,∥] Xian-He Bu,*[,†] and Pei-Xiang Lu*[,‡,⊥,#]

[†]School of Materials Science and Engineering; TKL of Metal and Molecule-Based Material Chemistry, Nankai University, Tianjin 300350, China

[‡]Wuhan National Laboratory for Optoelectronics and School of Physics, Huazhong University of Science and Technology, Wuhan 430074, China

[§]Engineering Research Institute, Jiangxi University of Science and Technology, Ganzhou 341000, China

[∥]Technical Institute of Physics and Chemistry, Chinese Academy of Sciences, Beijing 100190, China

[⊥]Hubei Key Laboratory of Optical Information and Pattern Recognition, Wuhan Institute of Technology, Wuhan 430205, China

[#]School of Physics and Electronic Engineering, Xinyang Normal University, Xinyang 464000, China

S *Supporting Information*

ABSTRACT: The flexible organic amine cations on the interfaces of two-dimensional (2D) hybrid organic−inorganic perovskite nanosheets could form relaxed structures, which would lead to exotic optoelectronic properties but are hard to understand. Here, the unusual interfacial relaxation of nanosheets exfoliated from an orthorhombic 2D lead halide perovskite, $[(C_6H_5CH_2NH_3)_2]PbCl_4$, is interrogated via ultrafast second-harmonic generation (SHG) spectroscopy. The in-plane SHG intensity anisotropy of these nanosheets is found to decrease with reducing layer thickness. Combined first-principles calculations and Monte Carlo simulations reveal that the induced second-order polarization arises primarily from the $(C_6H_5CH_2NH_3)^+$ cations; and these organic amine cations form significantly reorganized conformations with decreasing nanosheet thickness due to weakened van der Waals interactions. Because the orientations of organic components at the interface determine their electric properties and specifically the dipolar susceptibility, the resulting structure leads to striking changes in the SHG properties.

In two-dimensional (2D) hybrid organic−inorganic perovskites (HOIPs), semiconducting inorganic layers and capped organic dielectric layers are homogeneously integrated at a molecular level to form natural multiquantum wells.[1,2] Unlike conventional inorganic 2D materials, layered HOIPs offer tremendous possibilities for tuning their optoelectronic properties through varying both the chemical and quantum-mechanical degrees of freedom.[3−5] In particular, the abundant organic components and their delicate interplay with the halide quantum wells in these layered compounds could give rise to extraordinary properties.[6] Notably, the optoelectronic properties of these 2D HOIPs are determined by the semiconducting inorganic species, whereas their excitonic dynamics are largely dependent on the nature of charge-balancing organic amine cations.[7−9]

The significant structural flexibility enabled by capping organic species in these 2D halides leads to easy delamination with molecularly thin perovskite nanosheets. More importantly, the organic amine cations on the interfaces of these nanosheets could show structural relaxation at the nanoscale level due to the delicate alterations of van der Waals (VdW) interactions, which would result in unusual optoelectronic properties.[10,11] However, such local structural alterations and associated property changes induced by the VdW interactions are normally difficult to be fully characterized, and they are therefore much less explored. To facilitate their understanding, we take the advantage of SHG, which directly reflects the interactions between photons and local structures,[12−14] to reveal the delicate structural difference in the halide nanosheets with different thickness exfoliated from an orthorhombic 2D lead halide perovskite, $[(C_6H_5CH_2NH_3)_2]$-$PbCl_4$. Our optical experiments demonstrate that the striking changes in the anisotropy of SHG intensity between the *b*- and *c*-axes are strongly dependent on the nanosheets thickness. By carrying out density functional theory (DFT) calculations and Monte Carlo (MC) simulations, we show that the VdW interactions from flexible organic amine cations play a key role in governing this unusual behavior.

$[(C_6H_5CH_2NH_3)_2]PbCl_4$ crystallizes in a polar orthorhombic space group $Cmc2_1$ at ambient conditions with cell parameters of $a = 33.619(7)$, $b = 7.8195(12)$, and $c = 7.7282(13)$ Å. It has previously been reported to be ferroelectric and SHG-active in its bulk form.[15,16] The monolayer structure is displayed in the boxed part of Figure 1a, where adjacent $PbCl_6$ octahedra are connected through a corner-sharing mode along the *b*- and *c*-axes to form an inorganic $[PbCl_4]^{2-}$ sheet charge-compensated by the $(C_6H_5CH_2NH_3)^+$ cations attached. It is noteworthy that the orientation of $(C_6H_5CH_2NH_3)^+$ cation exhibits slight differences in the *b*- and *c*-axes (Figure S1). The thickness of the monolayer is about 1.67 nm. Adjacent monolayers are adhered via VdW

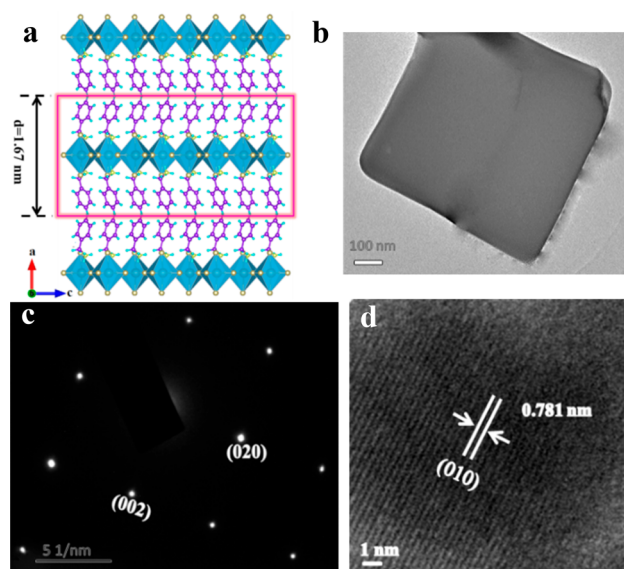**Figure 1.** (a) Crystal structure of $[(C_6H_5CH_2NH_3)_2]PbCl_4$ projected along *b*-axis. Color: C, purple; N, green; H, teal; Pb, blue; Cl, yellow. The thickness of the monolayer highlighted by the red box is about 1.67 nm. TEM bright-field image (b), SAED pattern (c), and high-resolution TEM image (d) of $[(C_6H_5CH_2NH_3)_2]PbCl_4$ nanosheets.

interactions from the neighboring $(C_6H_5CH_2NH_3)^+$ cations along the *a*-axis.

The $[(C_6H_5CH_2NH_3)_2]PbCl_4$ nanosheets were obtained by liquid-assisted exfoliation, and their crystallinity and morphology were characterized via transmission electron microscopy (TEM).

Delaminated nanosheets exhibit various thicknesses and their lateral dimensions range from a few hundreds of nanometers to a few tens of microns (Figures 1b and S2a). Selected-area electron diffraction (SAED) pattern demonstrates the high crystallinity of the exfoliated nanosheet (Figure 1c). The collected sharp diffraction spots correspond to (020) and (002) planes of the structure. Further high-resolution TEM images in Figure 1d show lattice fringes of about 0.781 nm, which corresponds to the *d*-spacing along the [010] direction.

Prior to SHG measurements, the thicknesses of nanosheets were quantified by atomic force microscopy (AFM). The thicknesses of nanosheets displayed in Figures 2a and S3 are, respectively, about 92.2, 58.3, 44.5, and 18.8 nm and 1210.7, 555.8, and 241.3 nm, with lateral sizes of approximately 10 μm. In order to investigate the polarization-dependent SHG response as a function of nanosheets thickness, the pumping laser was aligned to propagate perpendicular to the nanosheets (defined as *x*-axis or *a*-axis) and polarize along the nanosheets (in *yz*-plane or *bc*-plane). The SHG polarization properties of the above nanosheets were measured using an 820 nm laser facility (Figure S4a). Spectra of SHG signals located at around 410 nm from these nanosheets are displayed in Figures 2b and S4b. The thickness
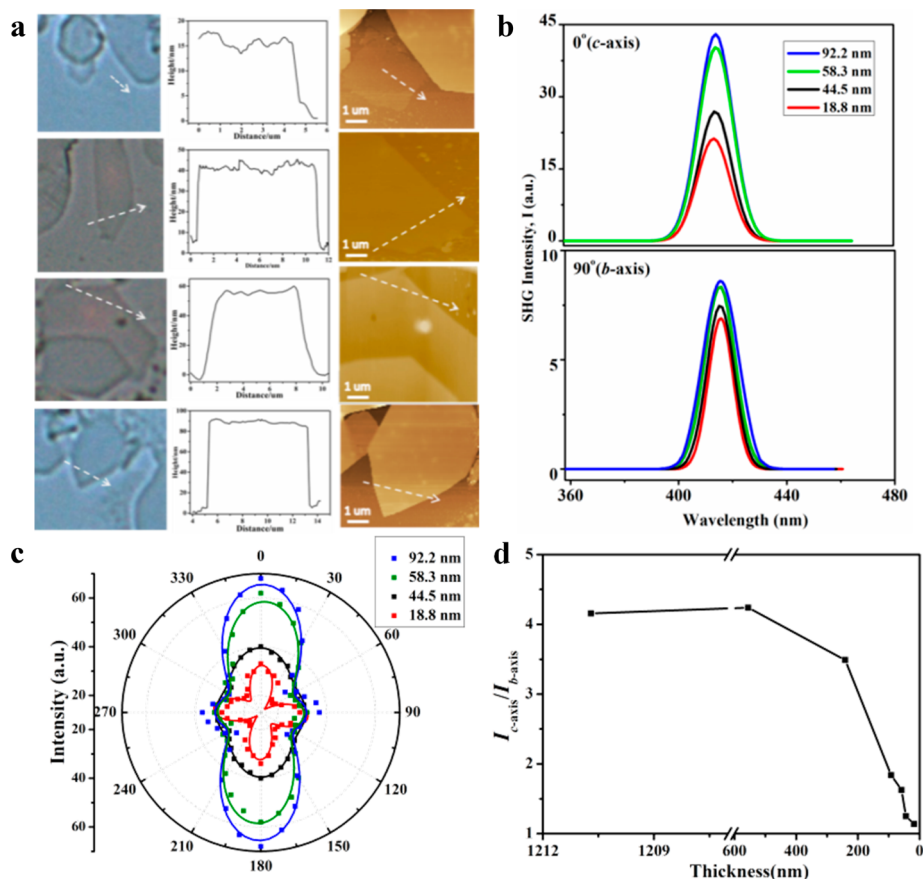

Figure 2. (a) Microscopic images (left), height profiles (middle), and topographies (right of measured nanosheets). (b) Spectra of SHG signals oriented to the *c*- (0°, above) and *b*-axes (90°, below) collected from nanosheets with different thickness, respectively. (c) Polar SHG intensity plots of the measured nanosheets. The dots represent the experimental data, and the solid curves indicate the theoretical fits. (d) SHG intensity anisotropy ($I_{c\text{-axis}}/I_{b\text{-axis}}$) dependent on the thickness of measured nanosheets.

ratio of measured nanosheets shown in Figure 2b is 1/0.63/0.48/ 0.20; however, the corresponding ratios of SHG intensity along c- and b-axes show reduced magnitudes of 1/0.91/0.59/0.49 and 1/ 0.87/0.87/0.78, respectively. The SHG intensities along both c- and b-axes gradually decrease with reducing nanosheets thickness; this to be expected since the measured polarization results from the superimposition of electric dipoles in these nanosheets and is hence proportional to the number of layers.[19]

All SHG polar plots are axi-symmetric along b- and c-axes as expected for an orthorhombic structure (Figures 2c and S4c). Notably, the in-plane anisotropy in SHG intensities (I), defined as the thickness reduces from 241.3 to 18.8 nm (Figure 2d). The detected I is proportional to the square of the induced second-order polarization (P) with the components P_x, P_y, and P_z, and the specific relationship can be described by the following equation for space group $Cmc2_1$:

$$\begin{bmatrix} P_x \\ P_y \\ P_z \end{bmatrix} = 2\varepsilon_0 \begin{bmatrix} 0 & 0 & 0 & 0 & d_{15} & 0 \\ 0 & 0 & 0 & d_{24} & 0 & 0 \\ d_{31} & d_{32} & d_{33} & 0 & 0 & 0 \end{bmatrix} \begin{bmatrix} E_x^2 \\ E_y^2 \\ E_z^2 \\ 2E_yE_z \\ 2E_xE_z \\ 2E_xE_y \end{bmatrix} \quad (1)$$

where d_{ij} is the second-order susceptibility tensor of measured nanosheets, and E_x, E_y, and E_z represent the components of electric field. The SHG intensity is expressed as

$$I_{SHG} \propto P_x^2 + P_y^2 + P_z^2$$
$$= (2d_{15}E_xE_z)^2 + (2d_{24}E_yE_z)^2$$
$$+ (d_{31}E_x^2 + d_{32}E_y^2 + d_{33}E_z^2)^2 \quad (2)$$

where $d_{15} = d_{31}$ and $d_{24} = d_{32}$ according to Kleinman symmetry.[17] Since the pumping laser propagates along the x- (or a-) axis, which induces polarized light within the yz- (or bc-) plane, and E_x is 0, the above formula can be simplified as

$$I_{SHG} \propto P_y^2 + P_z^2 = (2d_{24}E_yE_z)^2 + (d_{24}E_y^2 + d_{33}E_z^2)^2 \quad (3)$$

Accordingly, we can obtain the second-order nonlinear coefficients through fitting experimental SHG data. The obtained d_{33}/d_{24} ratios are, respectively, 1.46 and 1.17 for the 92.2 and 18.8 nm nanosheets, which agree well with the aforementioned in-plane anisotropy ratios of SHG intensities measured along the b- and c-axes (Figure 2b).

To understand the relationship between SHG anisotropy and nanosheet thickness, it is first necessary to determine the atomic origin of polarization characteristics for this 2D perovskite structure. The second-order nonlinear coefficients of the bulk structure were calculated using DFT,[18−21] which gave d_{24} and d_{33} values of −0.20 and −1.43 pm/V, respectively (Table 1). The d_{33}/d_{24} value of 7.15 is reasonably close to the value of 2.16 from experimentally measured 1210.7 nm sample approximating the bulk. In addition, the specific contributions from the $(C_6H_5CH_2NH_3)^+$ organic cation and $[PbCl_4]^{2-}$ were quantified using the real-space atom-cutting method.[22] Importantly, the results reveal that the contributions of $(C_6H_5CH_2NH_3)^+$ to the d_{24} and d_{33} coefficients are about 3.44 and 2.02 times those from

Table 1. Calculated Second-Order Nonlinear Coefficients of the Bulk Structure, Decomposed Organic $[(C_6H_5CH_2NH_3)_2]^{2+}$, and Inorganic $[PbCl_4]^{2-}$ Components by DFT

composition	d_{24}(pm/V)	d_{33}(pm/V)
$[(C_6H_5CH_2NH_3)_2]PbCl_4$	−0.20	−1.43
$[(C_6H_5CH_2NH_3)_2]^{2+}$	−0.31	−1.11
$[PbCl_4]^{2-}$	0.09	−0.55

$[PbCl_4]^{2-}$, which could lead to the aforementioned optical quantum effects.[10,11,23]

To explore the structural evolution in a simple way, MC simulations[24,25] were first performed on the nanosheets models with layer number (n) from 500 to 15 (the thinnest sample experimentally achieved), in which the effective interactions between layers were modeled using the Lennard-Jones potential:[26,27]

$$U = \sum_{i,j(i<j)} 4\varepsilon \left[\left(\frac{\sigma}{l_{ij}} \right)^{12} - \left(\frac{\sigma}{l_{ij}} \right)^6 \right] \quad (4)$$

where n denotes the layer number and ε represents the potential well depth of the two layers, σ stands for the finite distance at which the interlayer potential between the two layers is zero, and l_{ij} is the interlayer distance between the i and j layer.

The potential minima of multilayered structures were calculated, which gave the interlayer spacing l_n-MC for each n-layered nanosheet model. In Figure 3a, the interlayer spacing ratio between the n-layered structure and the bulk, l_n/l_{bulk}, is plotted in dependence of n. Strikingly, l_n/l_{bulk} monotonically increases by about 3.20% when n decreases from 500 to 15, indicating the increasing structural relaxation with reducing layer thickness. In MC simulations, $[(C_6H_5CH_2NH_3)_2]PbCl_4$ layers are regarded as rigid bodies, and local structural changes inside nanosheet models are unable to be reflected. First-principles calculations based on interlayer spacing ratios from MC were then performed, which reveal that both l_n/l_{bulk} and d_n/d_{bulk} (d_n and d_{bulk} are the thickness of a monolayer in the n-layered structure and the bulk, respectively) ratios exhibit a monotonically increasing tendency by about 0.94 and 2.16% when n decreases from 500 to 15 (Table S1). Such a structural relaxation is very likely to arise from the VdW interactions among nonadjacent monolayers, which are not usually considered in calculating energetics of 2D materials nanosheets. More importantly, the abundant VdW interactions in this layered perovskite are responsible for such a more significant quantum effect over conventional 2D materials. These results demonstrate that both the interlayer spacing and thickness in different multilayered nanosheets are not uniform but increase with decreasing layer number (Figure 3c).

To investigate the evolution of interlayer interactions with respect to layer thickness, the interlayer interaction energy, E_{inter}, was calculated. The E_{inter} value, calculated with dispersion corrections, decreases monotonically as n decreases, confirming the reduced interlayer interactions with decreasing layer number (Figure 3b). However, such a relationship reverses to an increasing trend if the energy related with dispersion terms in the Hamiltonian is discarded. Such a marked difference highlights the key role of the VdW interactions in reinforcing the formation of multilayered structures.

Further detailed analyses reveal the VdWs forces facilitated relaxation process of the $(C_6H_5CH_2NH_3)^+$ cation in optimized n-
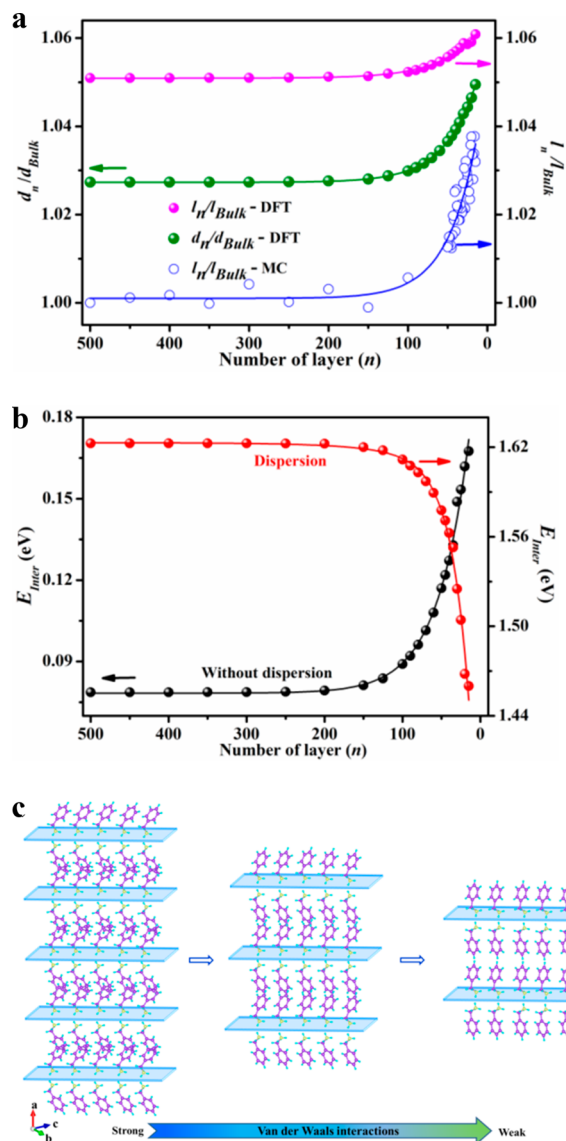
Figure 3. (a) Monolayer thickness ratio (d_n/d_{bulk}) and interlayer spacing ratio (l_n/l_{bulk}) as a function of layer number (n), calculated using MC and DFT methods. (b) Effective interaction energy in dependence of n calculated from DFT. (c) Schematic changes in the conformation of $(C_6H_5CH_2NH_3)^+$ cation and associated alterations of monolayer thickness in different multilayered nanosheets.

Figure 4. Dihedral angle ω (a) and θ and ϕ angles (b) as a function of n. (c) Schematic illustration of the conformational changes of $(C_6H_5CH_2NH_3)^+$ cation in the mono- (green) and multilayered (pink) structures. The black dashed arrows represent the axes formed by the benzyl plane. The green and pink dashed arrows, respectively, stand for the projections of $(C_6H_5CH_2NH_3)^+$ along b- and c-axes.

layered structures (Figures 3c and S5). Specifically, the angle (ω) between the $(C_6H_5CH_2NH_3)^+$ and bc-plane increases from 76.91° to 77.34° (by ∼0.5%) as n decreases from 500 to 15 (Figure 4a and Table S1). As the inorganic $[PbCl_4]^{2-}$ layer is rigid, it prevents significant changes of the negative charge distribution in response to layer thickness alterations. In this regard, the orientation changes of the organic amine cations, which dominate d_{33} and d_{24}, account for most of the changes in SHG properties. The angles between $(C_6H_5CH_2NH_3)^+$ and b-axis (θ) and between $(C_6H_5CH_2NH_3)^+$ and c-axis (ϕ) increase, respectively, from 39.40° to 39.55° (∼0.4%) and 47.40° to 47.76° (∼0.8%) when n decreases from 500 to 15 (Table S1). As seen in Figure 4c, the increase of θ and ϕ reduces the dipole projections along the b- and c-axes, which leads to the decreased polarization and corresponding reduced d_{24} and d_{33} values. However, the change in ϕ is about twice that in θ, which results in more pronounced reduction in d_{33} than d_{24}; hence, the decrease
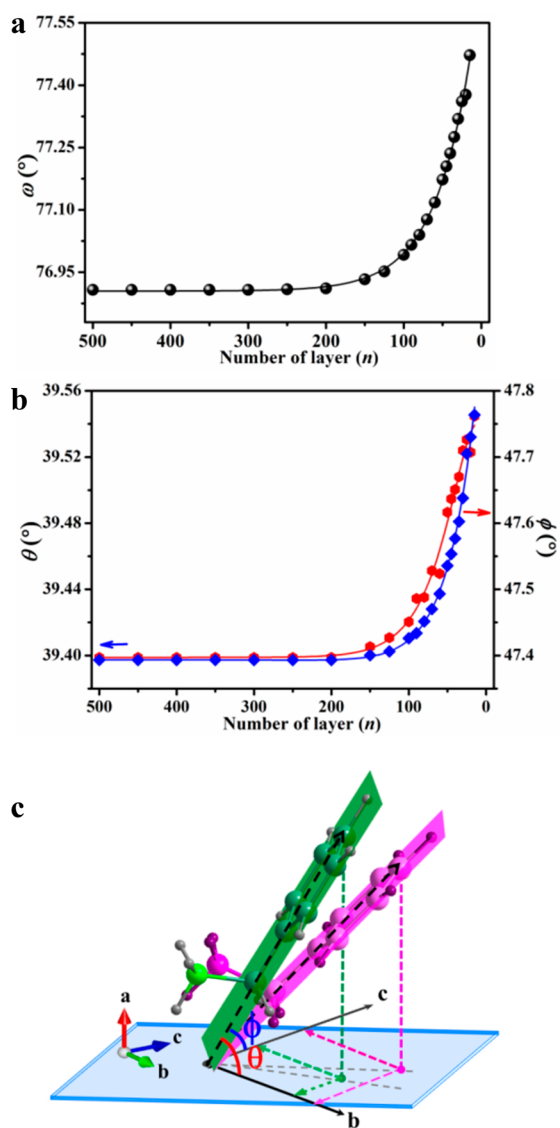
of d_{33}/d_{24} (Figure 2d). In other words, the reduction of VdW interactions with decreasing n is the primary cause of the decrease of SHG anisotropy.

In summary, we report the SHG properties of nanosheets exfoliated from an orthorhombic 2D hybrid perovskite $[(C_6H_5CH_2NH_3)_2]PbCl_4$. Our results show that the SHG intensities of these nanosheets increase with increasing layer thickness, whereas their in-plane anisotropies exhibit an inverse trend. With the aid of MC simulations and DFT calculations, we unveil that the conformational alterations of $(C_6H_5CH_2NH_3)^+$, which are due to the delicate changes of the VdW interactions, modulate the orientation of electric dipoles and corresponding SHG properties. Our work highlights the importance of dispersion forces in regulating physical properties of these quantum confined hybrid layered materials and also opens up opportunities for studying exotic properties by considering the

delicate interplay among multiple atomic bonding forces in 2D materials.[28,29]

■ ASSOCIATED CONTENT

ⓢ Supporting Information

The Supporting Information is available free of charge on the ACS Publications website at DOI: 10.1021/jacs.9b01874.

> Synthesis, second harmonic generation, Lennard-Jones potential calculations, density functional theory calculations, and some other supplementary data (PDF)

■ AUTHOR INFORMATION

Corresponding Authors

*wl276@nankai.edu.cn
*zslin@mail.ipc.ac.cn
*buxh@nankai.edu.cn
*lupeixiang@hust.edu.cn

ORCID

Xing-Xing Jiang: 0000-0001-6068-8773
Wei Li: 0000-0002-5277-6850
Zhe-Shuai Lin: 0000-0002-9829-9893
Xian-He Bu: 0000-0002-2646-7974

Author Contributions

[∇]These authors contributed equally: Wen-Juan Wei and Xing-Xing Jiang.

Notes

The authors declare no competing financial interest.

■ ACKNOWLEDGMENTS

■ REFERENCES

(1) Saparov, B.; Mitzi, D. B. Organic-inorganic perovskites: structural versatility for functional materials design. *Chem. Rev.* **2016**, *116*, 4558−4596.

(2) Stoumpos, C. C.; Cao, D. H.; Clark, D. J.; Young, J.; Rondinelli, J. M.; Jang, J. I.; Hupp, J. T.; Kanatzidis, M. G. Ruddlesden-Popper hybrid lead iodide perovskite 2D homologous semiconductors. *Chem. Mater.* **2016**, *28*, 2852−2867.

(3) Pedesseau, L.; Sapori, D.; Traore, B.; Robles, R.; Fang, H. H.; Loi, M. A.; Tsai, H.; Nie, W.; Blancon, J. C.; Neukirch, A.; Tretiak, S.; Mohite, A. D.; Katan, C.; Even, J.; Kepenekian, M. Advances and promises of layered halide hybrid perovskite semiconductors. *ACS Nano* **2016**, *10*, 9776−9786.

(4) Quintero-Bermudez, R.; Gold-Parker, A.; Proppe, A. H.; Munir, R.; Yang, Z.; Kelley, S. O.; Amassian, A.; Toney, M. F.; Sargent, E. H. Compositional and orientational control in metal halide perovskites of reduced dimensionality. *Nat. Mater.* **2018**, *17*, 900−907.

(5) Butler, K. T. The chemical forces underlying octahedral tilting in halide perovskites. *J. Mater. Chem. C* **2018**, *6*, 12045−12051.

(6) Traore, B.; Pedesseau, L.; Assam, L.; Che, X.; Blancon, J. C.; Tsai, H.; Nie, W.; Stoumpos, C. C.; Kanatzidis, M. G.; Tretiak, S.; Mohite, A. D.; Even, J.; Kepenekian, M.; Katan, C. Composite nature of layered hybrid perovskites: Assessment on quantum and dielectric confinements and band alignment. *ACS Nano* **2018**, *12*, 3321−3332.

(7) Quarti, C.; Marchal, N.; Beljonne, D. Tuning the optoelectronic properties of two-dimensional hybrid perovskite semiconductors with alkyl chain spacers. *J. Phys. Chem. Lett.* **2018**, *9*, 3416−3424.

(8) Zhang, S.; Lanty, G.; Lauret, J.-S.; Deleporte, E.; Audebert, P.; Galmiche, L. Synthesis and optical properties of novel organic-inorganic hybrid nanolayer structure semiconductors. *Acta Mater.* **2009**, *57*, 3301−3309.

(9) Kawano, N.; Koshimizu, M.; Sun, Y.; Yahaba, N.; Fujimoto, Y.; Yanagida, T.; Asai, K. Effects of organic moieties on luminescence properties of organic-inorganic layered perovskite-type compounds. *J. Phys. Chem. C* **2014**, *118*, 9101−9106.

(10) Dou, L.; Wong, A. B.; Yu, Y.; Lai, M.; Kornienko, N.; Eaton, S. W.; Fu, A.; Bischak, C. G.; Ma, J.; Ding, T. Atomically thin two-dimensional organic-inorganic hybrid perovskites. *Science* **2015**, *349*, 1518−1521.

(11) Leng, K.; Abdelwahab, I.; Verzhbitskiy, I.; Telychko, M.; Chu, L.; Fu, W.; Chi, X.; Guo, N.; Chen, Z.; Chen, Z.; Zhang, C.; Xu, Q. H.; Lu, J.; Chhowalla, M.; Eda, G.; Loh, K. P. Molecularly thin two-dimensional hybrid perovskites with tunable optoelectronic properties due to reversible surface relaxation. *Nat. Mater.* **2018**, *17*, 908.

(12) Yuan, C.; Li, X.; Semin, S.; Feng, Y.; Rasing, T.; Xu, J. Chiral lead halide perovskite nanowires for second-order nonlinear optics. *Nano Lett.* **2018**, *18*, 5411−5417.

(13) Autere, A.; Jussila, H.; Dai, Y.; Wang, Y.; Lipsanen, H.; Sun, Z. Nonlinear optics with 2D layered materials. *Adv. Mater.* **2018**, *30*, 1705963.

(14) Ye, H. Y.; Liao, W. Q.; Hu, C. L.; Zhang, Y.; You, Y. M.; Mao, J. G.; Xiong, R. G. Bandgap engineering of lead-halide perovskite-type ferroelectrics. *Adv. Mater.* **2016**, *28*, 2579−2586.

(15) Braun, M.; Frey, W. Crystal structure of bis (benzylammonium) lead tetrachloride,$(C_7H_7NH_3)_2PbCl_4$. *Z. Kristallogr. New Cryst. Struct.* **1999**, *214*, 331−332.

(16) Liao, W. Q.; Zhang, Y.; Hu, C. L.; Mao, J. G.; Ye, H. Y.; Li, P. F.; Huang, S. D.; Xiong, R. G. A lead-halide perovskite molecular ferroelectric semiconductor. *Nat. Commun.* **2015**, *6*, 7338.

(17) Kleinman, D. A. Nonlinear dielectric polarization in optical media. *Phys. Rev.* **1962**, *126*, 1977.

(18) Lin, Z.; Lin, J.; Wang, Z.; Chen, C.; Lee, M. H. Mechanism for linear and nonlinear optical effects in LiB_3O_5, CsB_3O_5, and $CsLiB_6O_{10}$ crystals. *Phys. Rev. B: Condens. Matter Mater. Phys.* **2000**, *62*, 1757.

(19) Jain, P.; Stroppa, A.; Nabok, D.; Marino, A.; Rubano, A.; Paparo, D.; Matsubara, M.; Nakotte, H.; Fiebig, M.; Picozzi, S.; Choi, E. S.; Cheetham, A. K.; Draxl, C.; Dalal, N. S.; Zapf, V. S. Switchable electric polarization and ferroelectric domains in a metal-organic-framework. *Npj Quant. Mater.* **2016**, *1*, 16012.

(20) Di Sante, D.; Stroppa, A.; Jain, P.; Picozzi, S. Tuning the ferroelectric polarization in a multiferroic metal-organic framework. *J. Am. Chem. Soc.* **2013**, *135*, 18126−18130.

(21) Xu, J.; Li, X.; Xiong, J.; Yuan, C.; Semin, S.; Rasing, T.; Bu, X.-H. *Adv. Mater.* **2019**, 1806736, DOI: 10.1002/adma.201806736. Published Online: March 18, 2019. https://onlinelibrary.wiley.com/doi/abs/10.1002/adma.201806736.

(22) Bai, L.; Lin, Z.; Wang, Z.; Chen, C.; Lee, M. H. Mechanism of linear and nonlinear optical effects of chalcopyrite $AgGaX_2$ (X= S, Se, and Te) crystals. *J. Chem. Phys.* **2004**, *120*, 8772−8778.

(23) Zhao, Y. Q.; Ma, Q. R.; Liu, B.; Yu, Z. L.; Yang, J.; Cai, M. Q. Layer-dependent transport and optoelectronic property in two-dimensional perovskite:$(PEA)_2PbI_4$. *Nanoscale* **2018**, *10*, 8677−8688.

(24) Gilks, W. R.; Richardson, S.; Spiegelhalter, D. *Markov Chain Monte Carlo in Practice*; Chapman and Hall/CRC, 1995.

(25) Elperin, T.; Gertsbakh, I.; Lomonosov, M. Estimation of network reliability using graph evolution models. *IEEE Trans. Reliab.* **1991**, *40*, 572−581.

(26) Geada, I. L.; Ramezani-Dakhel, H.; Jamil, T.; Sulpizi, M.; Heinz, H. Insight into induced charges at metal surfaces and biointerfaces using a polarizable Lennard-Jones potential. *Nat. Commun.* **2018**, *9*, 716.

(27) Heinz, H.; Vaia, R. A.; Farmer, B. L.; Naik, R. R. Accurate simulation of surfaces and interfaces of face-centered cubic metals using 12−6 and 9−6 Lennard-Jones potentials. *J. Phys. Chem. C* **2008**, *112*, 17281−17290.

(28) Blancon, J. C.; Stier, A. V.; Tsai, H.; Nie, W.; Stoumpos, C. C.; Traore, B.; Pedesseau, L.; Kepenekian, M.; Katsutani, F.; Noe, G. T.; Kono, J.; Tretiak, S.; Crooker, S. A.; Katan, C.; Kanatzidis, M. G.; Crochet, J. J.; Even, J.; Mohite, A. D. Scaling law for excitons in 2D perovskite quantum wells. *Nat. Commun.* **2018**, *9*, 2254.

(29) Kamminga, M. E.; Hidayat, R.; Baas, J.; Blake, G. R.; Palstra, T. T. M. Out-of-plane polarization in a layered manganese chloride hybrid. *APL Mater.* **2018**, *6*, 066106.